Vacuum ultraviolet excited state dynamics of the smallest ring, cyclopropane. II. Time-resolved photoelectron spectroscopy and ab initio dynamics

Michael R. Coates, Martin A. B. Larsen, Ruaridh Forbes, Simon P. Neville, Andrey E. Boguslavskiy, Iain Wilkinson, Theis I. Sølling, Rune Lausten, Albert Stolow, and Michael S. Schuurman

Citation: J. Chem. Phys. **149**, 144311 (2018); doi: 10.1063/1.5044402
View online: https://doi.org/10.1063/1.5044402
View Table of Contents: http://aip.scitation.org/toc/jcp/149/14
Published by the American Institute of Physics

Vacuum ultraviolet excited state dynamics of the smallest ring, cyclopropane. II. Time-resolved photoelectron spectroscopy and *ab initio* dynamics

Michael R. Coates,[1] Martin A. B. Larsen,[2] Ruaridh Forbes,[3,4] Simon P. Neville,[1] Andrey E. Boguslavskiy,[4,5] Iain Wilkinson,[6] Theis I. Sølling,[2] Rune Lausten,[5] Albert Stolow,[1,4,5] and Michael S. Schuurman[1,5]

[1]*Department of Chemistry and Biomolecular Sciences, University of Ottawa, 10 Marie Curie Drive, Ottawa, Ontario K1N 6N5, Canada*
[2]*Department of Chemistry, University of Copenhagen, 2100 Copenhagen Ø, Denmark*
[3]*Department of Physics and Astronomy, University College London, Gower Street, London WC1E 6BT, United Kingdom*
[4]*Department of Physics, University of Ottawa, 25 Templeton Street, Ottawa, Ontario K1N 6N5, Canada*
[5]*National Research Council of Canada, 100 Sussex Dr., Ottawa, Ontario K1A 0R6, Canada*
[6]*Helmholtz-Zentrum Berlin für Materialien und Energie GmbH Hahn-Meitner-Platz 1, D-14109 Berlin, Germany*

(Received 12 June 2018; accepted 17 September 2018; published online 12 October 2018)

The vacuum-ultraviolet photoinduced dynamics of cyclopropane (C_3H_6) were studied using time-resolved photoelectron spectroscopy (TRPES) in conjunction with *ab initio* quantum dynamics simulations. Following excitation at 160.8 nm, and subsequent probing via photoionization at 266.45 nm, the initially prepared wave packet is found to exhibit a fast decay (<100 fs) that is attributed to the rapid dissociation of C_3H_6 to ethylene (C_2H_4) and methylene (CH_2). The photodissociation process proceeds via concerted ring opening and C–C bond cleavage in the excited state. *Ab initio* multiple spawning simulations indicate that ring-opening occurs prior to dissociation. The dynamics simulations were subsequently employed to simulate a TRPES spectrum, which was found to be in excellent agreement with the experimental result. On the basis of this agreement, the fitted time constants of 35 ± 20 and 57 ± 35 fs were assigned to prompt (i) dissociation on the lowest-lying excited state, prepared directly by the pump pulse, and (ii) non-adiabatic relaxation from higher-lying excited states that lead to delayed dissociation, respectively. *Published by AIP Publishing.* https://doi.org/10.1063/1.5044402

I. INTRODUCTION

The photochemistry of cyclopropane and its substituted derivatives has been studied extensively for its use in synthetic organic chemistry.[1–3] This moiety is often bonded to larger chromophores in organic synthesis and facilitated isomerization and ring-expansion[1] upon irradiation with deep-ultraviolet radiation (up to 6.7 eV).[4–7] As the smallest organic ring, the excited states of cyclopropane and the cyclopropyl radical have been of interest for many years, with previous studies focusing on vibronic coupling in the lowest-energy excited states.[8–10] This is especially true of the cyclopropyl radical cation, which has been a subject of study for more than 45 years.[11–14] Despite the extensive literature describing the photochemistry of cyclopropane, to our knowledge, there exist no time-resolved studies of the excited state dynamics of this molecule.

Previous gas phase studies have shown that photolysis of cyclopropane occurs in vacuum-ultraviolet (VUV) for excitation energies ranging from 7.6 to 10.0 eV.[15–18] These reports highlight that branching between numerous reaction pathways can result, including the dissociation of cyclopropane, to yield ethylene and the methylene radical,

$$\text{c-}C_3H_6 \xrightarrow{h\nu} C_2H_4 + CH_2. \quad (1)$$

In one study, this pathway was found to account for 69% of the photoproducts following excitation at 163.4 nm.[17] The three remaining pathways observed are $CH_3 + C_2H_3$ (17%), H-loss (14%), and H_2 formation (1%). Here we consider excitation with 160.8 nm (7.71 eV) photons that populate a range of electronically excited states well above the $C_2H_4 + CH_2$ dissociation threshold that is estimated to occur at 3.72 eV.[18]

The ground state electronic configuration of cyclopropane is given by

$$[\text{core}](2a_1')^2(2e')^4(1a_2'')^2(3a_1')^2(1e'')^4(3e')^4,$$

where the highest occupied molecular orbital (HOMO), $3e'$, is a C–C σ-bonding orbital and the lowest energy virtual orbitals are of $3s(a_1')$, $3p_z(a_2'')$, and $3p_{x/y}(e')$ Rydberg character. For the sake of brevity, here and in the following, the label $3p_{x/y}$ is used as a shorthand for $3p_x/3p_y$. The identity of the $E'\sigma(3s)$ state as the lowest-lying state was confirmed by one- and two-photon absorption measurements.[19] While transition to the $\sigma 3s$ Rydberg state is dipole-allowed, the low oscillator strength of the transition has made experimental characterization of this state challenging. This transition has been observed in the 6.5-6.8 eV region both by direct absorption[19,20] and by resonance enhanced multi-photon ionization,[10,19] but with low intensity.

The two lowest-lying dipole allowed absorption bands with significant oscillator strength have their onset at 7.1 eV and exhibit broad maxima centered at 7.9 and 8.6 eV.[21,22] These two bands were attributed to the two Jahn-Teller (JT) split components of the $E'(\sigma 3p_{x/y})$ state. Previous assignments of the absorption spectrum have, however, neglected the effects of vibronic coupling. In a companion publication to Paper I,[23] new calculations of the absorption spectrum, which explicitly include the effects of vibronic coupling between the excited states, are presented. There it is conclusively demonstrated that intensity borrowing from the optically bright $E'(\sigma 3p_{x/y}) \leftarrow S_0$ transition by the dipole-forbidden $A_1'(\sigma 3p_{x/y}) \leftarrow S_0$ and $A_2'(\sigma 3p_{x/y}) \leftarrow S_0$ transitions gives rise to the majority of the intensity in the first two bands of the absorption spectrum. As discussed below, this new assignment of the spectrum has important implications for the analysis of the electronic character of the wave packet prepared following photoexcitation.

In the following, we present a joint experimental and theoretical study of the dynamics of cyclopropane following photoexcitation at 160.8 nm and using time-resolved photoelectron spectroscopy (TRPES)[24] to probe the evolution of the excited state wave packet. *Ab initio* multiple spawning (AIMS) computations are employed to both elucidate the underlying vibronic dynamics and simulate the TRPES spectrum.

II. EXPERIMENTAL AND THEORETICAL METHODS

A. Experimental

The femtosecond VUV pulse generation scheme employed in these experiments was described in detail previously.[25] In short, the laser system (Coherent Legend Elite Duo) employed throughout these experiments delivered 7.5 mJ pulses at 1 kHz, with a central frequency of 800 nm. A 3.25 mJ component of the total laser output was split to generate the pump and probe arms. The probe arm was frequency tripled by sum frequency mixing in two consecutive β-BaB_2O_4 (BBO) crystals, allowing for energies of 1 μJ per pulse. The pump was generated by four-wave mixing in Ar gas.[26] Specifically, the pump arm is split into two paths; one part was frequency tripled to 266 nm by a pair of consecutive BBO crystals and the other part is left as the fundamental at 800 nm. The resulting beams were focused and overlapped in a non-collinear fashion in an Ar gas cell, held at 43 mBar, to generate the 160.8 nm pump pulse and yield an energy per pulse close to 0.5 μJ. A set of dichroic mirrors having high reflectivity at 160 nm and high transmission at 266.45 nm and 800 nm were used to separate the residual driving beams in the wave mixing process and for subsequent recombination of the pump and probe laser pulses.

The pump and probe beams were mildly focused and collinearly combined along the optical axis of velocity map imaging (VMI) spectrometer.[27] Along this axis, the beams passed through a set of input baffles, the sample molecular beam, and a set of exit baffles. The baffles were incorporated in the spectrometer to help minimize the electron signals associated with scattered UV/VUV light. The pump-probe delay at the sample was controlled by a motorized delay stage (Newport XML210). The temporal overlap of the pump and probe pulses was found via non-resonant 1 + 1′ ionization of Xe. The time resolution was determined by fitting a Gaussian function to the temporal dependence of the non-resonant electron yield which resulted in a cross correlation duration of 105 fs full-width at half-maximum (FWHM). The splitting of the $^2P_{3/2}$ and $^2P_{1/2}$ lines in the ionic ground state in Xe also served as spectrometer energy calibration. The molecular beam was generated in a source chamber by expansion of a 5% mix of cyclopropane in He through an Even-Lavie valve at a stagnation pressure of 2 bars. The supersonic molecular beam was skimmed before entering the light-molecular beam interaction chamber and a stack of open aperture electrostatic lens plates. The molecular beam was injected along the axis of photoelectron projection, perpendicular to the pump and probe laser beam propagation. The accelerated photoelectrons were detected by a Microchannel Plate (MCP)-phosphor detector with the images recorded using a Charge-Coupled Device (CCD) camera. The recorded images were processed by a matrix inversion method[28] to obtain the inverse Abel transform. However, ionization of residual gas in the interaction chamber produced a non-negligible background signal which was corrected for by dynamically recording the background signal between gas pulses. This was done at each pump-probe delay for each scan in order to account for any time-dependent background signals. 30 identical scans of the pump-probe delay were averaged to produce the presented spectra.

B. *Ab initio* multiple spawning calculations

In the AIMS method,[29–31] the wavefunction *ansatz* is given by

$$|\Psi(\boldsymbol{R},\boldsymbol{r},t)\rangle = \sum_{I=1}^{n_s} |\psi_I(\boldsymbol{r},\boldsymbol{R})\rangle |\chi_I(\boldsymbol{R},t)\rangle. \tag{2}$$

Here, $\boldsymbol{r}$ and $\boldsymbol{R}$ denote the electronic and nuclear coordinates, respectively. The $|\psi_I(\boldsymbol{r},\boldsymbol{R})\rangle$ denote the adiabatic electronic states and $|\chi_I(\boldsymbol{R},t)\rangle$ is the nuclear wavefunction for the Ith electronic state. The nuclear wavefunctions are in turn expanded in terms of frozen Gaussian basis functions $|g_j^I\rangle$,

$$|\chi_I(\boldsymbol{R},t)\rangle = \sum_{j=1}^{N_I(t)} C_j^I(t) |g_j^I(\boldsymbol{R};\bar{\boldsymbol{R}}_j^I(t),\bar{\boldsymbol{P}}_j^I(t),\gamma_j^I(t),\alpha_j^I)\rangle. \tag{3}$$

Each Gaussian basis function depends parametrically on a time-dependent centroid position, $\bar{\boldsymbol{R}}_j^I$, momentum, $\bar{\boldsymbol{P}}_j^I$, and phase, γ_j^I, as well as a time-independent width, α_j^I. The positions and momenta are taken to evolve classically while the phases are propagated according to semi-classical equations of motion (EOMs).[32] The expansion coefficients C_j^I are determined variationally via the solution of the time-dependent Schrödinger equation. The number of Gaussian basis functions, $N_I(t)$, is time-dependent, with new basis functions created, or spawned, in regions of large derivative coupling in order to describe non-adiabatic transitions between adiabatic electronic states.[32]

C. Time-resolved photoelectron spectroscopy simulations

We consider ionization from a set $\left\{|\psi_I\rangle : I = 1, \ldots, n_s^0\right\}$ of N-electron states to a set $\{|\psi_\alpha\rangle : \alpha = 1, \ldots, n_s^+\}$ of $(N-1)$-electron states. We model the TRPES data as an incoherent sum of contributions from the relative probabilities of ionization, $W_{I\alpha}$, evaluated at the centres $\bar{\boldsymbol{R}}_j^I$ of the Gaussian basis functions in the AIMS dynamics calculations,

$$\sigma(E,t) = \sum_{I=1}^{n_s^0} \sum_{\alpha=1}^{n_s^+} \sum_{j=1}^{N_{I(t)}} \left|C_j^I(t)\right|^2 W_{I\alpha} \delta\left(E - \left(\omega - \Delta E_{I\alpha}(\bar{\boldsymbol{R}}_j^I(t))\right)\right). \tag{4}$$

Here, ω denotes the probe photon energy and $\Delta E_{I\alpha}$ is the vertical energy difference between the states $|\psi_I\rangle$ and $|\psi_\alpha\rangle$. The δ-function arises because we assume vertical ionization to occur. To proceed, we take the relative probabilities of ionization, $W_{I\alpha}$, to be proportional to the squares of the corresponding Dyson orbital norms, $\phi_{I\alpha}^D$,

$$W_{I\alpha} \propto ||\phi_{I\alpha}^D||^2, \tag{5}$$

$$\phi_{I\alpha}^D = \sqrt{N}\langle\psi_I|\psi_\alpha\rangle. \tag{6}$$

The approximation in Eq. (5) is known to hold well in the case of weak field ionization,[33] which is the situation considered in the present study.

The calculated TRPES data are convoluted with a Gaussian using a FWHM of 105 fs in the time domain and 0.23 eV in the energy domain. The time and energy convolutions correspond to the respective duration and energy spreads of the experimental pump and probe laser pulses, as determined in the cross correlation measurements.

D. Computational details

In the AIMS calculations, the adiabatic energies, energy gradients, and non-adiabatic couplings required to evaluate the EOMs were calculated at the multi-reference first-order configuration interaction (MR-FOCI) level of theory. The reference configurations and orbitals were taken from a complete active space self-consistent-field (CASSCF) calculation employing an active space including the orbitals $3e'(\sigma), 4a_1'(3s)$, $2a_2''(3p_z)$, and $4e'(3p_x, 3p_y)$. We denote this level of theory by CAS(4,6). In the CAS(4,6) calculations, state averaging was performed over the nine lowest singlet states, corresponding to $A_1'(\sigma^2), E'(\sigma 3s)$, $E''(\sigma 3p_z)$, $A_2'(\sigma 3p_{x/y})$, $A_1'(\sigma 3p_{x/y})$, and $E'(\sigma 3p_{x/y})$ at the Franck-Condon (FC) point. The level of theory is denoted by MR-FOCI(4,6). The aug-cc-pVDZ basis was used in all calculations. All electronic structure calculations were performed using the COLUMBUS set of programs.[34]

Initial positions and momenta were sampled from the harmonic ground vibrational state Wigner distribution, with the required normal modes and frequencies being calculated at the coupled-cluster with single, double, and perturbative triple excitations [CCSD(T)]/cc-pVTZ level of theory using the CFOUR set of programs.[35] A total of 25 initial basis functions were used with each propagated independently under the so-called independent first generation approximation.[32] A propagation time of 400 fs was used. At the end of the AIMS simulations, a total of 1260 basis functions had been spawned.

As a result of the limited accuracy of the computationally tractable MR-FOCI(4,6) calculations used in the AIMS calculations, the vertical ionization energies $\Delta E_{I\alpha}$ used in the simulation of the TRPES data are not sufficiently accurate to be used on their own. To correct for this, a constant shift of these terms was applied such that the calculated FC point S_1-to-D_0 ionization energy was brought into agreement with the value calculated at a higher level of theory. Specifically, this shift was calculated using energies calculated at the equation-of-motion coupled-cluster with single and double excitations (EOM-CCSD) level using the aug-cc-pVTZ basis. All EOM-CCSD calculations were performed using the CFOUR program.[35]

III. EXPERIMENTAL RESULTS

We first present our experimental TRPES results, which will subsequently be compared to AIMS simulations in Sec. IV. The pump (7.71 eV) and probe (4.65 eV) pulses combine to give a total photon energy of 12.36 eV, yielding the D_0 and D_1 cation states as open channels.[36] The adiabatic ionization energy of cyclopropane is 9.86 eV[37–39] and therefore a maximum photoelectron kinetic energy of 2.5 eV is expected. Figure 1(a) shows the TRPES spectrum measured following excitation at 7.71 eV. The spectrum exhibits two broad maxima, centered at 1.3 eV and 1.9 eV, which exhibit different temporal dynamics as a function of pump-probe delay. The integrated photoelectron signals and the time scales associated with the two bands are qualitatively very clear from the transients shown in Fig. 1(b). A time delay between the appearance of the two peaks in the TRPES data can clearly be seen. This could be interpreted as the initially excited state undergoing fast internal conversion (IC) to a lower excited state[40] and/or energy-lowering structural dynamics occurring within the initially excited state.

A 2D global fitting procedure was employed to investigate the detailed time-dependence of the photoelectron signal. We used the Levenberg-Marquardt fitting routine, with the experimental data ($S(E, \Delta t)$) described[41] by the following expression:

$$S(E,\Delta t) = \sum_{i=1}^{n} A_i(E) \cdot P_i(\Delta t) \otimes g(\Delta t), \tag{7}$$

where E is the kinetic energy of the photoelectron, Δt is the pump-probe time-delay, $g(\Delta t)$ is the experimental Gaussian instrument response or cross correlation function (105 fs FWHM), and $A_i(E)$ is the amplitude profile of the decay-associated photoelectron spectrum (DAS) of the ith decay channel with time-dependence $P_i(\Delta t) = \exp(-\Delta t/\tau_i)$. The global fit yielded two time-constants (i.e., $n = 2$) displayed in Table I; $\tau_1 = 35 \pm 20$ fs for the decay of the high kinetic energy peak and $\tau_2 = 57 \pm 35$ fs for the decay of the low kinetic energy peak. The DAS is shown in Fig. 2. The negative amplitude in the DAS associated with the 35 fs time constant has

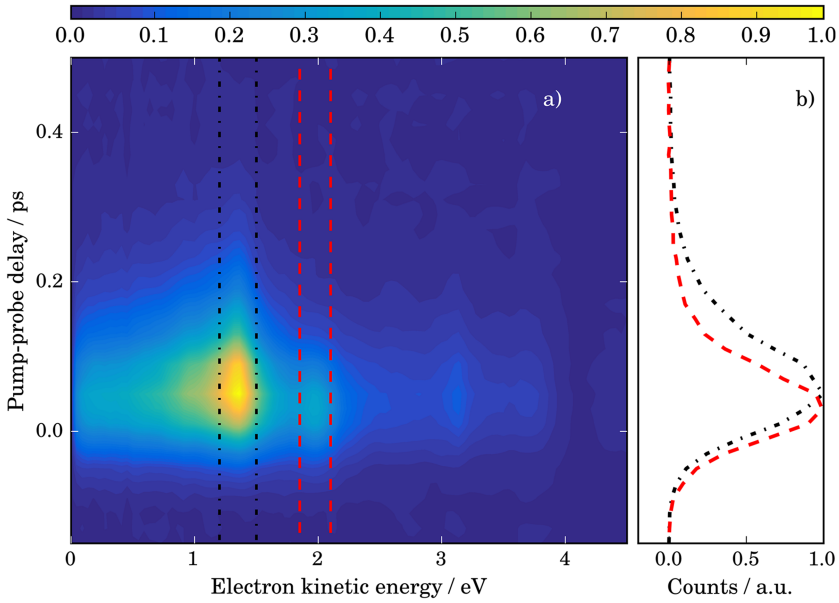

FIG. 1. (a) Time-resolved photoelectron spectroscopy (TRPES) spectrum of cyclopropane recorded using pump and probe wavelengths of 160.8 nm and 267 nm, respectively. (b) Integrated energy regions (black and red vertical lines) showing the pump-probe delay dependent yields.

TABLE I. Decay constants τ_1 and τ_2 from the 2D global fits to the experimental and simulated TRPES data. The error bars correspond to a 95% confidence interval from the 2D global fitting procedure.

	Experimental	Theoretical
τ_1 (fs)	35 ± 20	43 ± 20
τ_2 (fs)	57 ± 35	65 ± 30

negative values around 1.3 eV, whilst the DAS for the 57 fs time constant has positive values in this region. This is a clear indication of a sequential process in which the initial wave packet decays on a time scale of $\tau_1 = 35$ fs to a lower-energy state and/or nuclear coordinate distribution that in turn has a lifetime of $\tau_2 = 57$ fs.

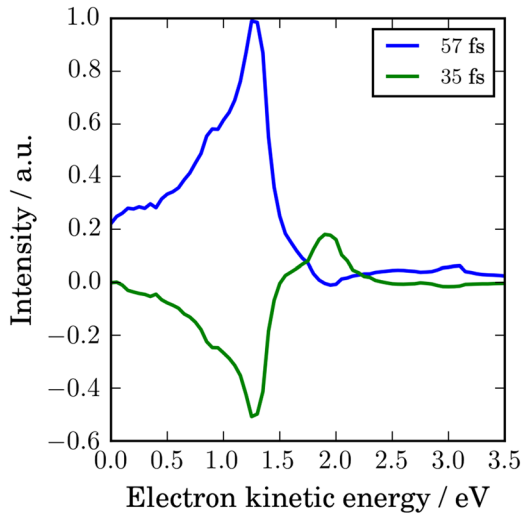

FIG. 2. Decay associated spectra from the 2D global fit to the experimental TRPES data. The negative amplitude associated with the 35 fs time constant is a clear indication of a sequential process.

IV. THEORETICAL RESULTS

A. Potential energy surfaces

Table II lists the vertical excitation energies of the first 5 singlet excited states calculated at the MR-FOCI/aug-cc-pVDZ level of theory. To assess the accuracy of the electronic structure method employed in the dynamics simulation, particularly the impact of employing a large (nine-) state average in the MCSCF computation, we will compare vertical excitation energies to the high-level aug-cc-pVTZ/CC3 and aug-cc-pVTZ/EOM-CCSD computations in Ref. 23. This comparison shows that the present vertical excitation energies differ from the benchmark level computations by ≈0.9 eV. This difference arises from the difficulty of the MR-FOCI wavefunction to describe the differential correlation effects between the valence ground state and the Rydberg excited state manifold. However, the dynamics of interest will be more sensitive to relative errors in energy *between* the excited states. On this metric, we see that the energies between the two methods are in quantitative agreement, with the MR-FOCI and CC3 and EOM-CCSD results displaying differences of ≈0.01 eV between the relative energies of the relevant excited states.

The first excited state is the $E'(\sigma 3s)$ state. At ≈0.45 eV above this energy lies a manifold of 4 electronic states that span only 0.66 eV. In order of increasing energy, these are

TABLE II. Vertical excitation energies at the Franck-Condon point calculated at the MR-FOCI(4,6)/aug-cc-pVDZ level of theory.

State	Symmetry	Character	ΔE (eV)
S_1	$^1E'$	$\sigma 3s$	6.73
S_2	$^1E''$	$\sigma 3p_z$	7.19
S_3	$^1A_2'$	$\sigma 3p_{x/y}$	7.30
S_4	$^1A_1'$	$\sigma 3p_{x/y}$	7.33
S_5	$^1E'$	$\sigma 3p_{x/y}$	7.35

the $^1E''(\sigma 3p_z)$, $^1A_2'(\sigma 3p_{x/y})$, $^1A_1'(\sigma 3p_{x/y})$, and $^1E'(\sigma 3p_{x/y})$ states. Upon JT distortion, the doubly degenerate states split, yielding a total of 8 non-degenerate excited adiabatic states. In the context of the excited state dynamics, the most important JT active modes correspond to asymmetric ring stretching and ring bending motions. Here, we will focus primarily on two nuclear degrees of freedom which serve to represent the dynamics involved: the angle bending coordinate, q_θ, and the CH_2 dissociation coordinate, q_{dissoc}. The definitions of these coordinates are given in Fig. 3.

Figure 4 shows the adiabatic potential energy surfaces (PESs) as a function of q_θ and q_{dissoc}, calculated at the MR-FOCI(4,6)/aug-cc-pVDZ level of theory. The lower adiabatic surfaces display barrierless large amplitude motion along these JT-active coordinates. Figure 4(a) evinces a flat manifold of potential surfaces along the q_θ coordinate, indicating that ring-opening is a largely barrierless process in the optically prepared excited states. Perhaps most importantly with regard to the excited state dynamics, as is shown in Fig. 4(b), the vertical excitation energies of all excited states lie above the barrier to the formation of ethylene (C_2H_4) and methylene (CH_2) in the S_1 state. Accordingly, dissociation would proceed promptly following population transfer to the S_1 state.

As evinced by Fig. 4(b), the potential energy surfaces employed in the dynamics simulations have minor discontinuities along the dissociation coordinate. These arise due to the σ^* orbital rotating into the large active space. While the classical energy of the trajectories in the simulation was conserved to 10^{-5} a.u., this discontinuity manifested as a small energy jump in the dissociation exit channel. Those trajectories undergoing this energy jump (exclusively on the adiabatic S_1 excited state) universally corresponded to dissociated products and were thus subsequently terminated.

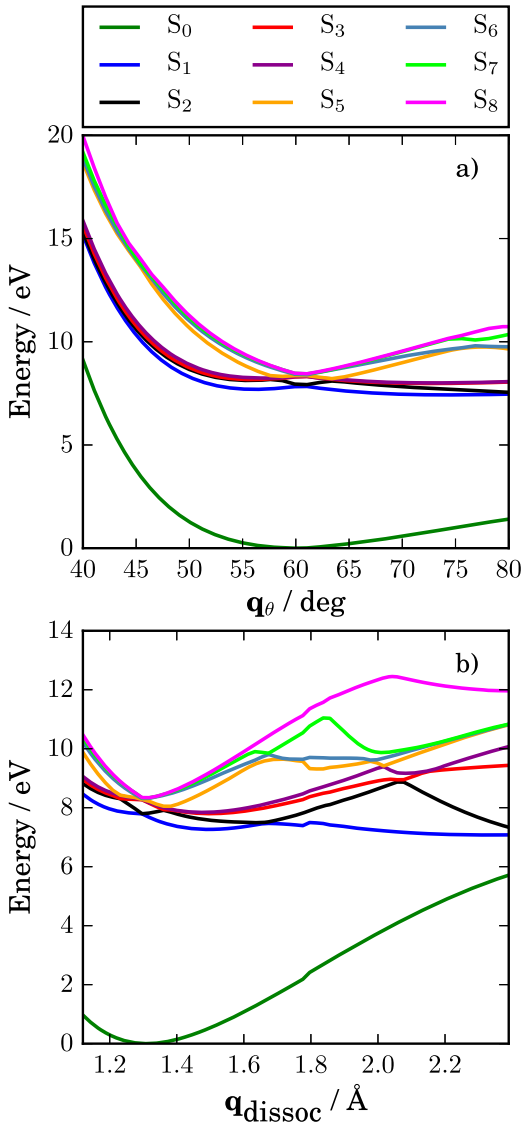

FIG. 4. Potential energy surface cuts along the ring opening (a), and bond dissociation (b) internal coordinates (see text for definitions). Both coordinates lift the degeneracy.

B. Photo-excitation: Initial state populations

Cyclopropane possesses a high density of low-lying vibronically coupled electronic states. In such a case, the initial state(s) prepared by a given pump pulse cannot be reliably estimated via an analysis of electronic transition dipoles and vertical excitation energies alone. The reason for this is that intensity borrowing effects may be operative, potentially leading to the population of optically dark electronic states. Indeed, our recent calculations, as discussed in the Paper I,[23] show that most of the intensity in the first two bands of cyclopropane's electronic absorption spectrum arises due to intensity borrowing from the optically bright $^1E'(\sigma 3p_{x/y})$ state by the

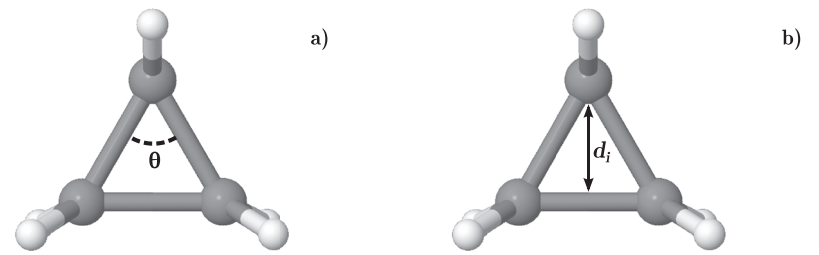

(i) $q_\theta{}^i = \theta_{C_jC_iC_k}$

(ii) $|q_\theta|_{\max} = \max[q_\theta{}^1, q_\theta{}^2, q_\theta{}^3]$

$X_{C_jC_k}$ = center of mass between C_j and C_k

(i) $q_{\text{dissoc}}{}^i = d_i = C_i - X_{C_jC_k}$

(ii) $|q_{\text{dissoc}}|_{\max} = \max[d_1, d_2, d_3]$

FIG. 3. The angle bending and dissociation coordinate definitions (a)(i) and (b)(i), respectively, were used to construct the potential energy surface cuts in Fig. 4. The maximum of the angle bending and dissociation coordinates as defined in (a)(ii) and (b)(ii), respectively, were used for all nuclear wave packet dynamics analyses in Figs. 5 and 8.

lower-lying optically dark states. Therefore, vibronic coupling effects must be included when estimating the initial state populations prepared by the experimental pump pulse. To do so, a model linear vibronic coupling Hamiltonian[42–44] was constructed which includes all first-order vibronic coupling terms between the first nine electronic states of cyclopropane. Initial state populations were then calculated by using the model Hamiltonian for a wave packet propagation calculation in which an initial ground state wavefunction was coupled to the excited state manifold via a laser pulse. By using a laser pulse parameterized to match the experimental pump pulse, the electronic state populations at the end of the wave packet propagation can be taken as estimates of the initial state populations prepared by the pump pulse. The wave packet propagation calculations were performed using the multiconfigurational time-dependent hartree (MCTDH) method[45] using a nine-state nine-mode model. The details of these calculations and the model Hamiltonian are given in the supplementary material of Ref. 23.

Using this approach, we found that only the S_1, S_2, S_3, and S_4 states are appreciably populated following excitation at 160.8 nm. This result is in direct contradiction with an analysis relying solely on transition dipole moments and vertical excitation energies, which would predict that the $^1E'(\sigma 3p_{x/y})$ is the initially prepared excited state. We do, however, have confidence in our results as the model Hamiltonian used is found to reproduce the experimental absorption spectrum to a high degree of accuracy.[23] Accordingly, in the following, we only consider excitation to these four states. The calculated relative populations of these states generated by the pump pulse are 0.33, 0.12, 0.30, and 0.25, respectively.

C. Wave packet dynamics simulation

Guided by the initial state populations calculated from the MCTDH calculations, AIMS simulations were performed with initial states corresponding to each of the S_1, S_2, S_3, and S_4 states.

Each wave packet propagation was performed independently and the results incoherently averaged using weights corresponding to the calculated initial state populations to give the final results. We first consider the one-dimensional reduced nuclear densities calculated from the AIMS simulations. These were calculated using the Monte-Carlo procedure detailed in Ref. 46. In Fig. 5(a), we show the calculated reduced densities for the angle bending coordinate as a function of time. It is predicted that ring opening occurs rapidly following photoexcitation, with direct ring opening first occurring within 50 fs. The remaining part of the wave packet undergoes a single revival back to the FC region after 80 fs, but then subsequently delocalizes over a wide range of angles greater than 100°.

Figure 5(b) shows the calculated reduced densities for the CH_2 dissociation coordinate. Similar to the ring bending coordinate, a bifurcation of the wave packet is found to occur, with one component undergoing rapid dissociation in under 50 fs and a second component undergoing a classical-like revival back toward the FC region before becoming delocalized along the dissociation coordinate. The horizontal dashed line in

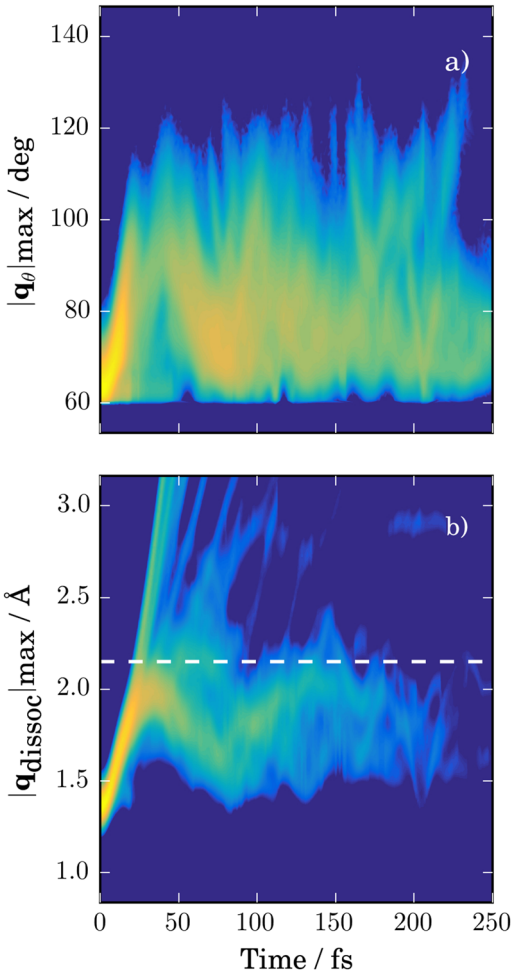

FIG. 5. One-dimensional reduced nuclear densities calculated from the AIMS simulations. (a) The angle bending coordinate. (b) The dissociation coordinate.

Fig. 5(b) marks the value of the dissociation coordinate beyond which the asymptotic region (dissociation limit) of the potential lies. Here, dissociation is defined as the distance between the centres of mass of the C_2H_4 and CH_2 fragments being greater than $|q_{dissoc}|_{max}$ = 2.1 Å. The picture which emerges is one in which CH_2 rapidly departs from a C_2H_4 co-fragment during a concerted ring-opening and bond stretching process.

Shown in Fig. 6(a) are the adiabatic state populations calculated from the AIMS simulations. The wave packet spans multiple electronic states, primarily S_1–S_4. However, the population on S_3 and S_4 decays almost immediately to S_2 and subsequently S_1. The latter displays a sudden increase in population around 25 fs corresponding to ring opened cyclopropane being transferred to S_1. Population on the ground adiabatic state begins to grow starting around 25 fs and continues to do so until the end of the simulation. Interestingly, there is a revival in S_2 population beginning around 50 fs which corresponds to a revival of the wave packet to the FC region, which is characterized by smaller bond angles and bond lengths as shown in Fig. 5 around 80 fs.

Figure 6(b) shows the calculated time-dependent probability of dissociation to form C_2H_4 and CH_2. It is predicted that cyclopropane begins to dissociate within 20 fs and that

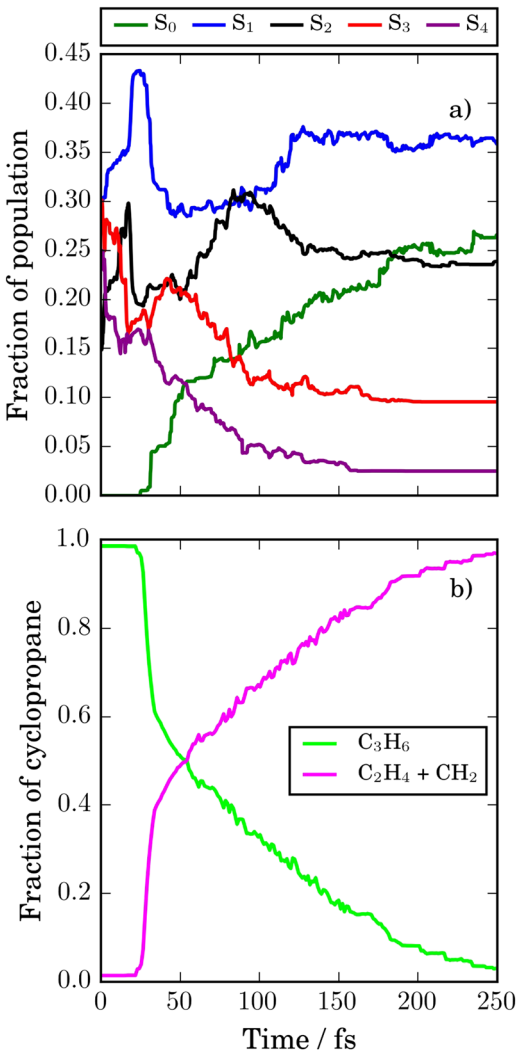

FIG. 6. Panel (a) shows the time evolution of the adiabatic state populations as obtained from the AIMS simulation. Panel (b) illustrates the fraction of the wave packet characterized by molecular C_3H_6 vs. dissociated C_2H_4 and CH_2 as a function of time.

dissociation is virtually complete by 250 fs. Finally, we note that the AIMS simulations predict that dissociation predominantly occurs on S_1, with population transfer to S_0 and S_2 largely occurring after the molecular system is already in the dissociation exit channel.

D. TRPES simulation

The TRPES data calculated from the AIMS simulations are shown in Fig. 7(a). The calculated spectrum contains two peaks centered at 1.3 and 1.9 eV, in excellent agreement with the experimental TRPES data. A fit to the computed spectrum was performed using the same 2D global fitting algorithm employed in the analysis of the experimental spectrum (see Sec. III). The fit residuals of both the experimental and calculated TRPES data are included in the supplementary material. The time constants derived from the fits to both the experimental and calculated TRPES data are given in Table I. The agreement between the time constants derived from the calculated and experimental TRPES spectra is quantitative and gives us confidence in the accuracy of the underlying AIMS dynamics simulations.

To shed light on the dynamical processes underlying the two time constants, we consider the contributions to the calculated TRPES data from: (i) the geometries at the centres of the Gaussian basis functions that contribute to each of the two bands and (ii) the contribution of each electronic state to the TRPES data. In the following, we label the region around the band centered at 1.9 eV as region I and the region around the band at 1.3 eV as region II.

In Figs. 7(b)–7(e), we show the contributions to the calculated TRPES spectrum from each of the excited states S_1, S_2, S_3, and S_4. As the figure shows, the higher energy peak in region I is due almost exclusively to ionization of S_3 and S_4, whereas the lower energy peak in region II contains contributions from all four adiabatic electronic states.

The two bands may be further characterized by analyzing the geometries $\bar{\boldsymbol{R}}_j^I$ at the centres of the Gaussian basis functions which give rise to the different regions in the calculated TRPES data. Specifically, for each Gaussian basis function contributing to the signal in each of regions I and II, we determine the value of the internal coordinates q_θ and q_{dissoc} at the centre of the basis function and histogram these values to determine the nuclear character of the wave packet giving rise to each region. The results of this computation are shown in Fig. 8. It can clearly be seen that region I is characterized mainly by geometries in the vicinity of the FC region ($q_\theta = 60°$ and $q_{\text{dissoc}} = 1.4$ Å). Conversely, we find that region II in the TRPES spectrum arises predominantly due to the components of the wave packet corresponding to structures significantly

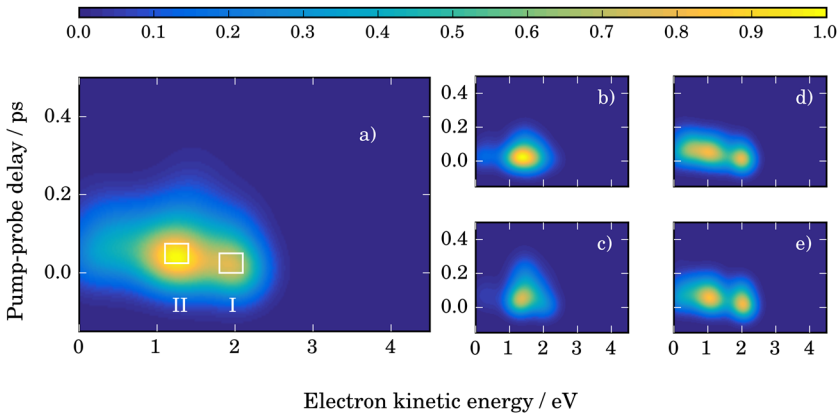

FIG. 7. (a) TRPES data calculated from the results of the AIMS simulations. Shown alongside are the contributions to the total spectrum from each electronic state: (b) S_1, (c) S_2, (d) S_3, and (e) S_4. All spectra are displayed with the same colourmap.

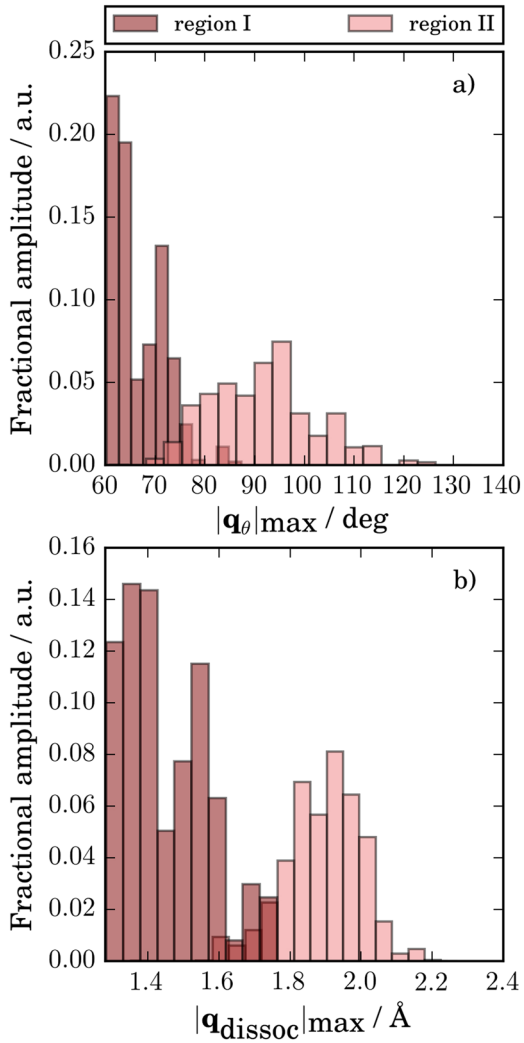

FIG. 8. Histogram of ring opening (a) and dissociation (b) coordinates for regions I and II (shown in Fig. 7) of the simulated TRPES spectrum.

displaced from the FC region. This is highlighted in Fig. 8 by a shift of the distribution to larger values of both internal coordinates.

V. DISCUSSION

The AIMS simulations predict that the dynamics immediately following photoexcitation at 160.8 nm involve nuclear motion in each of the excited states, including barrierless ring-opening and large-amplitude C–C stretching vibrations. These structural deformations occur on all the prepared excited states (S_1–S_4) and are accompanied by rapid non-adiabatic transitions to the lowest-lying adiabatic electronic states (S_1, S_2) from the higher-lying states (S_3, S_4). The population in the lower-lying states subsequently undergoes barrierless dissociation to produce C_2H_4 + CH_2. The ground electronic state population which begins to accumulate after about ~30 fs is found to arise solely due to electronic relaxation in the dissociation exit channel, as described by Fig. 6(b).

Significantly, each of these processes is encoded in the experimental TRPES data, and comparison with AIMS simulations allows the nature of the excited state dynamics to be extracted from these results. Based on the analysis of the simulated TRPES in terms of the underlying trajectory simulations in Sec. IV D, the interpretation of the experimental TRPES that emerges is thus: the band in region I corresponds to ionization of the components of initially excited wave packet in states S_3 and S_4. Region II at short times corresponds exclusively to ionization from S_1 and S_2, but this component of the wave packet rapidly dissociates. As the wave packet evolves, the population in the S_3 and S_4 states undergoes large amplitude structural relaxation, which increases the ionization potential (yielding lower kinetic energy electrons) and results in an increased signal in region II. This interpretation is confirmed by Fig. 8 which shows the lower energy band arising from more highly JT distorted geometries involving large amplitude motion corresponding to ring-opening and C–C bond elongation.

The time scale for dissociation (<100 fs) is captured by the time constant fits to both the experimental and simulated data. As the molecule undergoes barrierless dissociation to C_2H_4 + CH_2, the instantaneous vertical ionization potential increases until single-photon ionization is no longer possible with a 4.65 eV probe photon and the photoionization cross section becomes correspondingly small. To be clear, the predicted photo-products from the proposed dynamical pathway cannot be ionized via one-photon ionization using the present pump-probe scheme and are thus not readily observable in this experiment. However, the quantitative agreement between the experimentally determined time constants and the corresponding parameters extracted from the spectrum generated from high level *ab initio* dynamics engender confidence in the present assignment. The main products observed in previous studies of the gas-phase photolysis, C_2H_4 + CH_2, have ionization energies of 10.40 eV[47] and 10.51 eV,[48] respectively, and would thus require ionization with 3 probe photons from their ground state. For the low probe laser intensities used in the current experiments, such channels were not observed.

The detailed results of our study are in general agreement with previous experimental studies which determined the photodissociation branching ratios following excitation at 163.4 nm.[17] In that report, the authors found that dissociation to C_2H_4 + CH_2 formed the dominant dissociation channel, accounting for 69% of the product yield. Three other channels observed involved the formation of CH_3+C_2H_3 (17% product yield), as well as H-loss (14%), and H_2 formation (1%). The investigators questioned whether the breaking of the C–C bonds to form the major dissociation products occurred simultaneously or was preceded by ring-opening. Our results confirm that it is the latter: the excited molecule first undergoes large amplitude motion, which includes ring-opening, before ultimately dissociating.

We note that the simulations reported here have found C_2H_4 + CH_2 to be the *only* product channel accessed via photoexcitation. However, since the present calculations exclusively investigated the nonadiabatic dynamics that result following photoexcitation, only those reaction products formed on the exited state, or promptly upon relaxation to the ground adiabatic state, would be observed in the simulations. The formation of C_2H_4 + CH_2 and other species via statistical dissociation from the hot ground state was not considered here.

VI. CONCLUSION

The current study finds that the photoinitiated dynamics of cyclopropane, following excitation near the maximum of the lowest lying absorption band at 160.8 nm, are characterized by rapid ring opening and dissociation to ethylene and methylene. While both these motions are initiated immediately upon excitation, the shorter time scale for ring-opening ensures that this process precedes dissociation. On the basis of quantitatively accurate simulations of the absorption spectrum, we can definitively state that the wave packet prepared by the pump process is of mixed electronic character and arises due to the strong vibronic coupling between the optically bright $^1E'$ and the lower-lying Rydberg states. That component of the wave packet which is prepared directly on the lowest lying 3s(S_1) state dissociates promptly, whereas those components of higher excited electronic character first undergo nonradiative decay to the lower adiabatic states before dissociating. Interestingly, both the structural and electronic relaxation dynamics give rise to distinct spectral features in the TRPES data, the assignment of which is enabled by high level *ab initio* simulations of the excited state dynamics and TRPES spectrum. Those components of the wave packet that correspond to higher-lying excited states at short times, prepared directly by the photoabsorption process, give rise to the photoelectron band at 1.9 eV, while a time delayed band around 1.3 eV arises following large amplitude nuclear displacements and non-radiative decay. The simulated spectrum shows that this lower-energy band also overlaps with the ionization signal from the initially prepared S_1 and S_2 states. The ethylene and methylene photoproducts are formed on the electronically excited S_1 state, but, as previous studies have shown, any excited state C_2H_4 product will rapidly undergo internal conversion to the ground electronic state. The degree of agreement between the simulated and experimentally determined TRPES spectra is impressive and has allowed for the unusually fine-grained assignment of all the main features of the time-resolved spectrum.

SUPPLEMENTARY MATERIAL

See supplementary material for details of both the quantum dynamics simulations and the global fits of the experimental and simulated TRPES.

ACKNOWLEDGMENTS

A.S. and M.S.S. thank the Natural Science and Engineering Research Council (NSERC) Discovery Grants program for financial support. R.F. is grateful to the Engineering and Physical Sciences Research Council (EPSRC) for a research studentship. We thank Varun Makhija (Ottawa) and Kevin Veyrinas (Bordeaux) for their contributions to the experimental development.

[1]H. N. C. Wong, M. Y. Hon, C. W. Tse, Y. C. Yip, J. Tanko, and T. Hudlicky, Chem. Rev. **89**, 165 (1989).
[2]K. Mizuno, N. Ichinose, and Y. Yoshimi, J. Photochem. Photobiol., C **1**, 167 (2000).
[3]N. Hoffmann, Chem. Rev. **108**, 1052 (2008).
[4]R. Srinivasan and J. A. Ors, J. Org. Chem. **44**, 3426 (1979).
[5]R. Srinivasan, T. Baum, and J. A. Ors, Tetrahedron Lett. **22**, 4795 (1981).
[6]T. Baum, A. Rossi, and R. Srinivasan, JACS **107**, 4411 (1985).
[7]W. J. Leigh and R. Srinivasan, Acc. Chem. Res. **20**, 107 (1987).
[8]W. Duch and G. A. Segal, J. Chem. Phys. **79**, 2951 (1983).
[9]W. Duch and G. A. Segal, J. Chem. Phys. **84**, 544 (1986).
[10]J. W. Zwanziger, A. Ghelichkhani, and E. R. Grant, J. Chem. Phys. **89**, 4012 (1988).
[11]C. Rowland, Chem. Phys. Lett. **9**, 169 (1971).
[12]K. Krogh-Jespersen and H. D. Roth, JACS **114**, 8388 (1992).
[13]D. J. Mann and W. L. Hase, JACS **124**, 3208 (2002).
[14]Z. Li, X. Chen, X. Shan, T. Liu, and K. Xu, J. Chem. Phys. **130**, 054302 (2009).
[15]C. L. Currie, H. Okabe, and J. R. McNesby, J. Phys. Chem. **67**, 1494 (1963).
[16]A. A. Scala and P. Ausloos, J. Chem. Phys. **49**, 2282 (1968).
[17]S. Kazuhiko, O. Kin-ichi, and I. Tanaka, Bull. Chem. Soc. Jpn. **48**, 1974 (1975).
[18]C. C. Wang, Y. T. Lee, J. J. Lin, J. Shu, Y.-Y. Lee, and X. Yang, J. Chem. Phys. **117**, 153 (2002).
[19]M. B. Robin and N. A. Kuebler, J. Chem. Phys. **69**, 806 (1978).
[20]P. Wagner and A. B. F. Duncan, J. Chem. Phys. **21**, 516 (1953).
[21]M. Gingell, N. J. Mason, I. C. Walker, G. Marston, H. Zhao, and M. R. F. Siggel, J. Phys. B: At., Mol. Opt. Phys. **32**, 2729 (1999).
[22]I. C. Walker, D. M. P. Holland, D. A. Shaw, I. J. McEwen, and M. F. Guest, J. Phys. B: At., Mol. Opt. Phys. **40**, 1875 (2007).
[23]S. P. Neville, A. Stolow, and M. S. Schuurman, J. Chem. Phys. **149**, 144310 (2018).
[24]A. Stolow, A. E. Bragg, and D. M. Neumark, Chem. Rev. **104**, 1719 (2004).
[25]R. Forbes, V. Makhija, K. Véyrinas, A. Stolow, J. W. L. Lee, M. Burt, M. Brouard, C. Vallance, I. Wilkinson, R. Lausten, and P. Hockett, J. Chem. Phys. **147**, 013911 (2017).
[26]M. Ghotbi, M. Beutler, and F. Noack, Opt. Lett. **35**, 3492 (2010).
[27]A. T. J. B. Eppink and D. H. Parker, Rev. Sci. Instrum. **68**, 3477 (1997).
[28]Y. T. Cho and S.-J. Na, Meas. Sci. Technol. **16**, 878 (2005).
[29]T. J. Martínez, M. Ben-Nun, and R. D. Levine, J. Phys. Chem. **100**, 7884 (1996).
[30]T. J. Martínez, M. Ben-Nun, and R. D. Levine, J. Phys. Chem. A **101**, 6389 (1997).
[31]M. Ben-Nun, J. Quenneville, and T. J. Martínez, J. Phys. Chem. A **104**, 5161 (2000).
[32]M. Ben-Nun and T. J. Martínez, Adv. Chem. Phys. **121**, 439 (2002).
[33]B. T. Pickup, Chem. Phys. **19**, 193 (1977).
[34]H. Lischka, R. Shepard, I. Shavitt, R. M. Pitzer, M. Dallos, T. Mller, P. G. Szalay, F. B. Brown, R. Ahlrichs, H. J. Böhm, A. Chang, D. C. Comeau, R. Gdanitz, H. Dachsel, C. Ehrhardt, M. Ernzerhof, P. Höchtl, S. Irle, G. Kedziora, T. Kovar, V. Parasuk, M. J. M. Pepper, P. Scharf, H. Schiffer, M. Schindler, M. Schler, M. Seth, E. A. Stahlberg, J.-G. Zhao, S. Yabushita, Z. Zhang, M. Barbatti, S. Matsika, M. S. Schuurman, D. R. Yarkony, S. R. Brozell, E. V. Beck, J.-P. Blaudeau, M. Ruckenbauer, B. Sellner, F. Plasser, and J. J. Szymczak, COLUMBUS an *ab initio* electronic structure program, release 7.0.
[35]J. F. Stanton, J. Gauss, M. E. Harding, P. G. Szalay, A. A. Auer, R. J. Bartlett, U. Benedikt, C. Berger, D. E. Bernholdt, Y. J. Bomble, L. Cheng, O. Christiansen, M. Heckert, O. Heun, C. Huber, T. C. Jagau, D. Jonsson, J. Juslius, K. Klein, W. J. Lauderdale, D. A. Matthews, T. Metzroth, L. A. Mück, D. P. O'Neill, D. R. Price, E. Prochnow, C. Puzzarini, K. Ruud, F. Schiffmann, W. Schwalbach, C. Simmons, S. Stopkowicz, A. Tajti, J. Vázquez, F. Wang, and J. D. Watts, CFOUR, Coupled-Cluster techniques for Computational Chemistry, a quantum-chemical program package, see http://www.cfour.de.
[36]D. Holland, L. Karlsson, and K. Siegbahn, J. Electron Spectrosc. Relat. Phenom. **125**, 57 (2002).
[37]H. Basch, M. B. Robin, N. A. Kuebler, C. Baker, and D. W. Turner, J. Chem. Phys. **51**, 52 (1969).
[38]F. Leng and G. Nyberg, J. Electron Spectrosc. Relat. Phenom. **11**, 293 (1977).
[39]P. Keller, J. Taylor, T. A. Carlson, T. Whitley, and F. Grimm, Chem. Phys. **99**, 317 (1985).

[40]S.-H. Lee, K.-C. Tang, I.-C. Chen, M. Schmitt, J. P. Shaffer, T. Schultz, J. G. Underwood, M. Z. Zgierski, and A. Stolow, J. Phys. Chem. A **106**, 8979 (2002).
[41]O. Schalk, A. E. Boguslavskiy, and A. Stolow, J. Phys. Chem. A **114**, 4058 (2010).
[42]L. S. Cederbaum, H. Köppel, and W. Domcke, Int. J. Quantum Chem. **20**(S15), 251 (1981).
[43]H. Köppel, W. Domcke, and L. S. Cederbaum, Adv. Chem. Phys. **57**, 59 (1984).
[44]H. Köppel, W. Domcke, and L. S. Cederbaum, in *Conical Intersections: Electronic Structure, Dynamics & Spectroscopy* (World Scientific Publishing, 2004), Vol. 15, Chap. 7, p. 323.
[45]M. H. Beck, A. Jäckle, G. A. Worth, and H.-D. Meyer, Phys. Rep. **324**, 1 (2000).
[46]J. D. Coe, B. G. Levine, and T. J. Martínez, J. Phys. Chem. A **111**, 11302 (2007).
[47]G. Herzberg, Can. J. Phys. **39**, 1511 (1961).
[48]B. A. Williams and T. A. Cool, J. Chem. Phys. **94**, 6358 (1991).